

# Effect of Space Dimensions on Equilibrium Solutions of Cahn–Hilliard and Conservative Allen–Cahn Equations

Hyun Geun Lee<sup>1</sup>, Junxiang Yang<sup>2</sup>, Jintae Park<sup>2</sup>  
and Junseok Kim<sup>2,\*</sup>

<sup>1</sup> Department of Mathematics, Kwangwoon University, Seoul 01897, Republic of Korea

<sup>2</sup> Department of Mathematics, Korea University, Seoul 02841, Republic of Korea

Received 8 October 2019; Accepted (in revised version) 26 December 2019

---

**Abstract.** In this study, we investigate the effect of space dimensions on the equilibrium solutions of the Cahn–Hilliard (CH) and conservative Allen–Cahn (CAC) equations in one, two, and three dimensions. The CH and CAC equations are fourth-order parabolic partial and second-order integro-partial differential equations, respectively. The former is used to model phase separation in binary mixtures, and the latter is used to model mean curvature flow with conserved mass. Both equations have been used for modeling various interface problems. To study the space-dimension effect on both the equations, we consider the equilibrium solution profiles for symmetric, radially symmetric, and spherically symmetric drop shapes. We highlight the different dynamics obtained from the CH and CAC equations. In particular, we find that there is a large difference between the solutions obtained from these equations in three-dimensional space.

**AMS subject classifications:** 65M55, 65N06, 76D05

**Key words:** Cahn–Hilliard equation, conservative Allen–Cahn equation, equilibrium solution, finite difference method, multigrid method.

---

## 1. Introduction

In this study, we investigate the effect of space dimensions on the equilibrium solutions of the Cahn–Hilliard (CH) and conservative Allen–Cahn (CAC) equations in one, two, and three dimensions. The CH equation is given as

$$\frac{\partial \phi}{\partial t}(\mathbf{x}, t) = \Delta \mu(\mathbf{x}, t), \quad \mathbf{x} \in \Omega, \quad t > 0, \quad (1.1a)$$

$$\mu(\mathbf{x}, t) = F'(\phi(\mathbf{x}, t)) - \epsilon^2 \Delta \phi(\mathbf{x}, t), \quad (1.1b)$$

---

\*Corresponding author. Email address: cfdkim@korea.ac.kr (J. Kim)

$$\mathbf{n} \cdot \nabla \phi(\mathbf{x}, t) = \mathbf{n} \cdot \nabla \mu(\mathbf{x}, t) = 0, \quad \mathbf{x} \in \partial\Omega, \quad t > 0, \quad (1.1c)$$

where the order parameter  $\phi(\mathbf{x}, t)$  is the difference between two concentrations in a binary mixture in the domain  $\Omega \subset \mathbb{R}^d$  ( $d = 1, 2, 3$ ).  $F(\phi) = 0.25(\phi^2 - 1)^2$  is the free-energy density,  $\epsilon$  is a positive constant related to the interfacial thickness, and  $\mathbf{n}$  is the outward normal vector at the boundary. The CH equation was introduced to model phase separation phenomena in binary alloys [1]. A review paper [2] that documents the physical, mathematical, and numerical derivations of the CH equation is available. The CAC equation is given as

$$\frac{\partial \phi}{\partial t}(\mathbf{x}, t) = -\frac{F'(\phi(\mathbf{x}, t))}{\epsilon^2} + \Delta \phi(\mathbf{x}, t) + \beta(t) \sqrt{F(\phi(\mathbf{x}, t))}, \quad \mathbf{x} \in \Omega, \quad t > 0, \quad (1.2a)$$

$$\mathbf{n} \cdot \nabla \phi(\mathbf{x}, t) = 0, \quad \mathbf{x} \in \partial\Omega, \quad t > 0, \quad (1.2b)$$

where

$$\beta(t) = \int_{\Omega} F'(\phi(\mathbf{x}, t)) d\mathbf{x} / \left[ \epsilon^2 \int_{\Omega} \sqrt{F(\phi(\mathbf{x}, t))} d\mathbf{x} \right].$$

This equation is a second-order integro-partial differential equation, which is used for modeling mean curvature flows under the assumption of conservation of mass [3]. Both the equations and their modified forms can be used to model various interface problems in phase separation, fluids, topology optimization, tumor growth, image segmentation, phase field crystals, and so on [4–11]. In [12], the CH and CAC equations were compared as phase models, and the different dynamics between the two equations were specifically depicted. Please refer to [12] for further information.

The primary objective of this study is to investigate equilibrium solutions of the two equations in one, two, and three dimensions. In particular, we highlight the different dynamics of the CH and CAC equations.

The remainder of this paper is organized as follows: In Section 2, we describe the numerical solution algorithms of the CH and CAC equations. In Section 3, we present the numerical experiments. Finally, the conclusions are presented in Section 4.

## 2. Numerical solution

In this section, we consider numerical solutions in symmetric, radially symmetric, and spherically symmetric forms. The symmetric form of the CH equation (1.1a) and (1.1b) is as follows:

$$\phi_t(r, t) = \frac{1}{r^{d-1}} [r^{d-1} \mu_r(r, t)]_r, \quad r \in \Omega, \quad t > 0, \quad (2.1a)$$

$$\mu(r, t) = F'(\phi(r, t)) - \frac{\epsilon^2}{r^{d-1}} [r^{d-1} \phi_r(r, t)]_r, \quad (2.1b)$$

where  $d$  is the space dimension. We discretize the CH equation (2.1a) and (2.1b) in  $\Omega = (0, a)$ . Let  $N_r$  be a positive even integer,  $h = a/N_r$  be the uniform mesh size,

$\Omega_h = \{r_i : r_i = (i - 0.5)h, 1 \leq i \leq N_r\}$  be the set of cell-centers, and  $t^n = n\Delta t$ . Let  $\phi_i^n$  and  $\mu_i^n$  be approximations of  $\phi(r_i, t^n)$  and  $\mu(r_i, t^n)$ , respectively. Further, we discretize Eqs. (2.1a) and (2.1b) in time using a nonlinear splitting algorithm [13]:

$$\frac{\phi_i^{n+1} - \phi_i^n}{\Delta t} = \Delta_h \mu_i^{n+1}, \quad (2.2a)$$

$$\mu_i^{n+1} = (\phi_i^{n+1})^3 - \phi_i^n - \epsilon^2 \Delta_h \phi_i^{n+1}, \quad (2.2b)$$

where

$$\Delta_h \phi_i^{n+1} = [r_{i+1/2}^{d-1}(\phi_{i+1}^{n+1} - \phi_i^{n+1}) - r_{i-1/2}^{d-1}(\phi_i^{n+1} - \phi_{i-1}^{n+1})]/(r_i^{d-1}h^2).$$

Eq. (1.1c) shows that the homogeneous Neumann boundary conditions for both  $\phi$  and  $\mu$  are to be used. The resultant system of discrete equations is solved by using a multigrid method [14]. There have been several multigrid solutions for the CH equation [15, 16]; therefore, we do not provide the complete descriptions of the solution algorithms. However, the core part of the multigrid algorithm, i.e., the relaxation part, is presented. First, we rewrite Eqs. (2.2a) and (2.2b) as follows:

$$\frac{\phi_i^{n+1}}{\Delta t} + \frac{r_{i+1/2}^{d-1} + r_{i-1/2}^{d-1}}{r_i^{d-1}h^2} \mu_i^{n+1} = \frac{\phi_i^n}{\Delta t} + \frac{r_{i+1/2}^{d-1}}{r_i^{d-1}h^2} \mu_{i+1}^{n+1} + \frac{r_{i-1/2}^{d-1}}{r_i^{d-1}h^2} \mu_{i-1}^{n+1}, \quad (2.3a)$$

$$\begin{aligned} & - (\phi_i^{n+1})^3 - \epsilon^2 \frac{r_{i+1/2}^{d-1} + r_{i-1/2}^{d-1}}{r_i^{d-1}h^2} \phi_i^{n+1} + \mu_i^{n+1} \\ & = -\phi_i^n - \epsilon^2 \frac{r_{i+1/2}^{d-1}}{r_i^{d-1}h^2} \phi_{i+1}^{n+1} - \epsilon^2 \frac{r_{i-1/2}^{d-1}}{r_i^{d-1}h^2} \phi_{i-1}^{n+1}. \end{aligned} \quad (2.3b)$$

Next, we linearize the nonlinear term and apply a Gauss–Seidel iterative scheme:

$$\begin{aligned} & \frac{1}{\Delta t} \phi_i^{n+1,m+1} + \frac{r_{i+1/2}^{d-1} + r_{i-1/2}^{d-1}}{r_i^{d-1}h^2} \mu_i^{n+1,m+1} \\ & = \frac{\phi_i^n}{\Delta t} + \frac{r_{i+1/2}^{d-1}}{r_i^{d-1}h^2} \mu_{i+1}^{n+1,m} + \frac{r_{i-1/2}^{d-1}}{r_i^{d-1}h^2} \mu_{i-1}^{n+1,m+1}, \end{aligned} \quad (2.4a)$$

$$\begin{aligned} & - \left[ 3(\phi_i^{n+1,m})^2 + \epsilon^2 \frac{r_{i+1/2}^{d-1} + r_{i-1/2}^{d-1}}{r_i^{d-1}h^2} \right] \phi_i^{n+1,m+1} + \mu_i^{n+1,m+1} \\ & = -\phi_i^n - 2(\phi_i^{n+1,m})^3 - \epsilon^2 \frac{r_{i+1/2}^{d-1}}{r_i^{d-1}h^2} \phi_{i+1}^{n+1,m} - \epsilon^2 \frac{r_{i-1/2}^{d-1}}{r_i^{d-1}h^2} \phi_{i-1}^{n+1,m+1}, \end{aligned} \quad (2.4b)$$

where  $\phi_i^{n+1,m+1}$  and  $\phi_i^{n+1,m}$  are the solutions after and before an iteration, respectively. We solve Eqs. (2.4a) and (2.4b) by using a  $2 \times 2$  matrix inversion for each  $i$ . The complete description of the multigrid method for the CH equation is available in [15].

Now, we describe a numerical solution for the CAC equation (1.2) in the symmetric form:

$$\phi_t(r, t) = -\frac{F'(\phi(r, t))}{\epsilon^2} + \frac{1}{r^{d-1}}[r^{d-1}\phi_r(r, t)]_r + \beta(t)\sqrt{F(\phi(r, t))}. \quad (2.5)$$

We use the hybrid method proposed in [17] for Eq. (2.5). This method is based on an operator-splitting technique. We numerically solve Eq. (2.5) by successively solving a sequence of simpler problems:

$$\phi_t(r, t) = \frac{1}{r^{d-1}}[r^{d-1}\phi_r(r, t)]_r, \quad (2.6a)$$

$$\phi_t(r, t) = -\frac{F'(\phi(r, t))}{\epsilon^2}, \quad (2.6b)$$

$$\phi_t(r, t) = \beta(t)\sqrt{F(\phi(r, t))}. \quad (2.6c)$$

By applying the backward Euler's method as well as the multigrid method [14] and using the homogeneous Neumann boundary condition (1.2b), we solve Eq. (2.6a):

$$\frac{\phi_i^{n+1,1} - \phi_i^n}{\Delta t} = [r_{i+1/2}^{d-1}(\phi_{i+1}^{n+1,1} - \phi_i^{n+1,1}) - r_{i-1/2}^{d-1}(\phi_i^{n+1,1} - \phi_{i-1}^{n+1,1})]/(r_i^{d-1}h^2).$$

The analytic solution of Eq. (2.6b) is obtained using the method of separation of variables:

$$\phi_i^{n+1,2} = \frac{\phi_i^{n+1,1}}{\sqrt{e^{-2\Delta t/\epsilon^2} + (\phi_i^{n+1,1})^2 (1 - e^{-2\Delta t/\epsilon^2})}}, \quad (2.7a)$$

$$\phi_i^{n+1} = \phi_i^{n+1,2} + \Delta t\beta^{n+1,2}\sqrt{F(\phi_i^{n+1,2})}, \quad (2.7b)$$

where

$$\beta^{n+1,2} = \frac{1}{\Delta t} \sum_{i=1}^{N_r} [\alpha(r_i)(\phi_i^0 - \phi_i^{n+1,2})h] \bigg/ \sum_{i=1}^{N_r} [\alpha(r_i)\sqrt{F(\phi_i^{n+1,2})}h], \quad (2.8)$$

and where the scaling factor,  $\alpha(r)$ , is given by

$$\alpha(r) = \begin{cases} 1, & \text{if } d = 1, \\ 2\pi r, & \text{if } d = 2, \\ 4\pi r^2, & \text{if } d = 3. \end{cases} \quad (2.9)$$

More details about the hybrid method can be found in [17]. In addition, a higher-order and mass-conservative method for the CAC equation can be referred to from [18]. Furthermore, we refer to a recent article [19] for benchmark problems for the AC and CH dynamics.

### 3. Numerical results and discussion

Unless otherwise specified, we use the notation  $\epsilon = \epsilon_s = hs/[2\sqrt{2}\tanh^{-1}(0.9)]$ , which ensures that the number of grid points across the interfacial regions (e.g.,  $|\phi| \leq 0.9$ ) is approximately  $s$  [20].

#### 3.1. Cahn–Hilliard equation

We consider the effect of the initial condition on the equilibrium-state configuration in the computational domain  $\Omega = (0, 1)$  with 64 grid points. Here, we use  $h = 1/64$ ,  $\epsilon = \epsilon_4$ , and  $\Delta t = 0.1h^2$ . We consider the initial conditions to be

$$\phi(r, 0) = \begin{cases} 1, & \text{if } r \leq qh, \\ -1, & \text{otherwise,} \end{cases} \quad (3.1)$$

where  $q$  is an integer. Fig. 1(a) shows the initial condition with  $q = 7$ . We define a numerical equilibrium solution if the discrete  $l_2$ -norm of the difference between the two consecutive time step solutions is less than  $10^{-6}$ , i.e.,  $\|\phi^{n+1} - \phi^n\|_2 < 10^{-6}$ . Figs. 1(b),

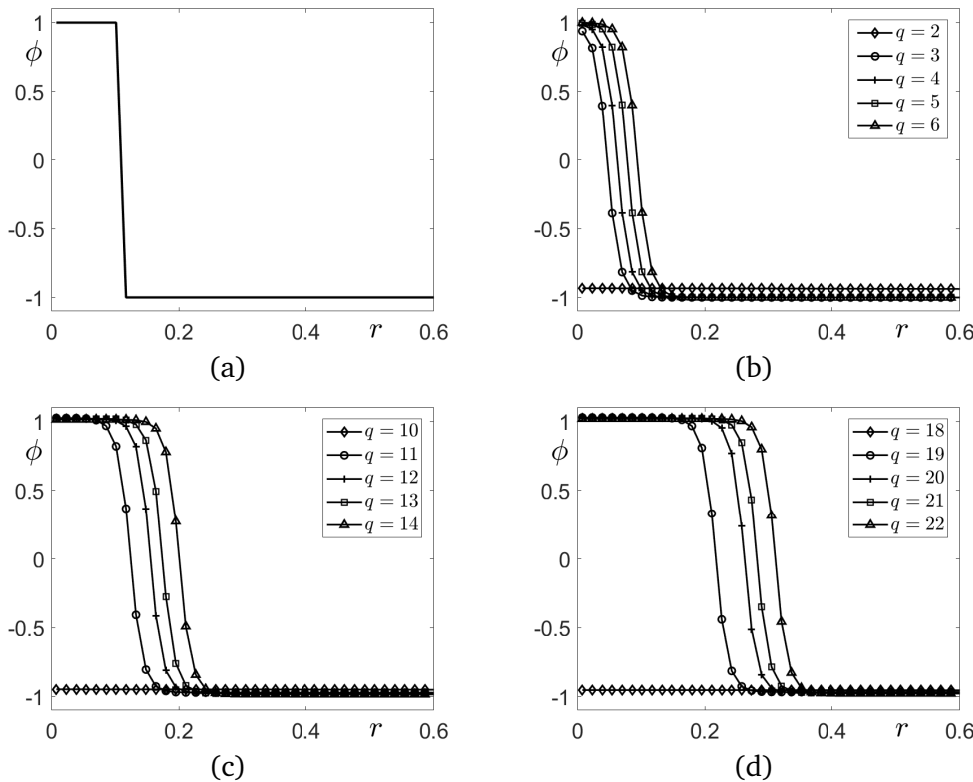


Figure 1: (a) Initial configuration with  $q = 7$ . (b), (c), and (d) depict the one-, two-, and three-dimensional numerical equilibrium solutions with different values of  $q$ , respectively.

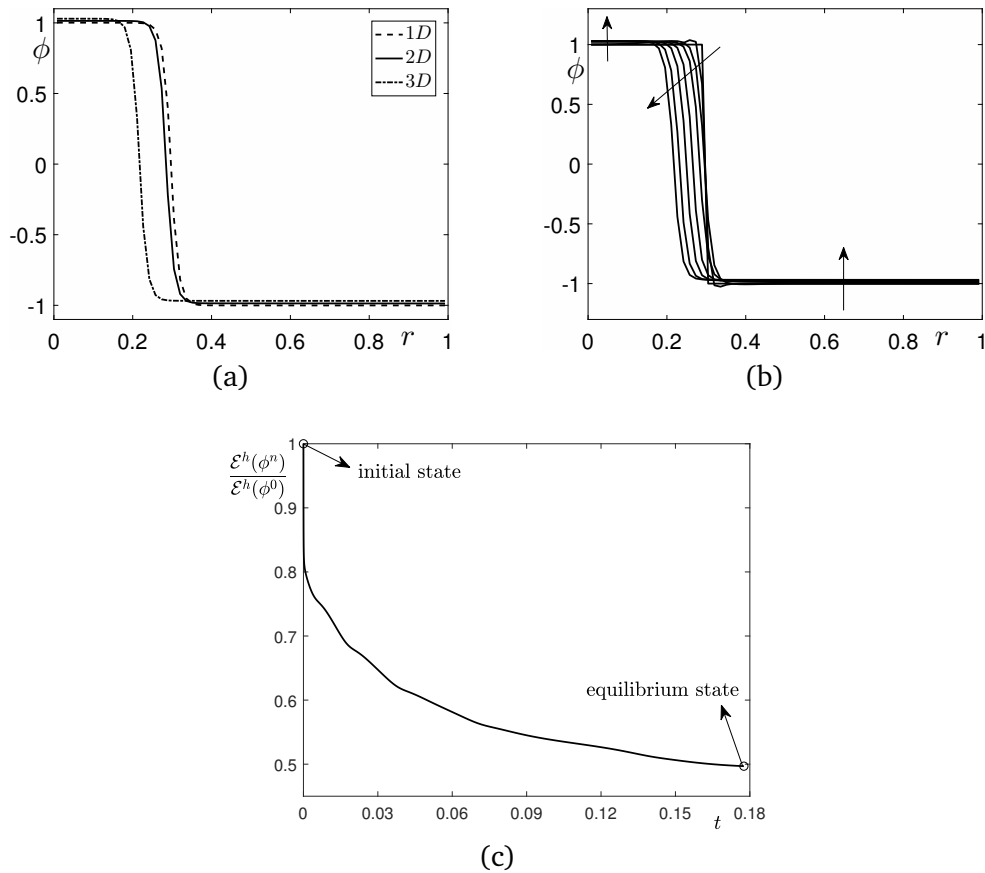


Figure 2: (a) Comparison between equilibrium solutions of one-, two-, and three-dimensional space with  $q = 19$ . (b) Temporal evolution of the numerical solution in three-dimensional space. The arrows indicate the direction of evolution. (c) Temporal evolution of normalized total energy with respect to the phase evolution in (b).

(c), and (d) show the one-, two-, and three-dimensional numerical equilibrium solutions with different values of  $q$ , respectively. From the results, we observe that for a small number of grid points, almost all constant solutions are equilibrium solutions. We can also infer that the minimum value of  $q$ , which yields a non-constant solution increases as the space dimension increases from 1D to 3D, i.e.,  $q = 3$ ,  $q = 11$ , and  $q = 19$ . Note that in the three-dimensional case with  $\epsilon_4$ , we need at least 38 grid points for a drop because it is spherically symmetric. In contrast, for less than 38 grid points, we obtain a flat solution instead of a drop shape. This is a very important finding, and it suggests that a sufficiently high resolution is required to simulate three-dimensional two-phase fluid flows using the CH equation.

Fig. 2(a) depicts the difference between the equilibrium solutions in one-, two-, and three-dimensional space with  $q = 19$ . In particular, for the three-dimensional case shown in Fig. 2(b), the drop shrinks substantially from the initial profile through a

Table 1:  $(p, q)$  for various  $\epsilon$  values, where  $p$  is the number of grid points satisfying  $\phi \geq -0.9$  and  $q$  is the minimum value of the integer required to preserve a drop shape in the equilibrium state.

Case	$\epsilon = \epsilon_4$	$\epsilon = \epsilon_6$	$\epsilon = \epsilon_8$	$\epsilon = \epsilon_{10}$	$\epsilon = \epsilon_{12}$
1D	(5, 3)	(7, 4)	(9, 5)	(10, 5)	(12, 6)
2D	(10, 11)	(13, 13)	(14, 14)	(19, 16)	(21, 17)
3D	(16, 19)	(21, 22)	(21, 23)	(26, 25)	(28, 26)

shift of the phase-field to a negative one. This result implies that, to set a drop in the three-dimensional space, we need to consider the shrinkage of the drop from an initial setting. For the CH model, the total energy can be reduced by shrinking the interface while simultaneously shifting the bulk  $\phi$  slightly away from the initial value from  $-1$  to  $1$  (see Fig. 2(b)). Fig. 2(c) illustrates the temporal evolution of total energy according to the evolution of  $\phi$  in Fig. 2(b). We can find that the total energy is decreasing in time.

Table 1 lists  $(p, q)$  for various  $\epsilon$  values, where  $p$  is the number of grid points satisfying  $\phi \geq -0.9$ , and  $q$  is the minimum value of the integer required to preserve a drop shape in the equilibrium state. Because the system is symmetric, we need double the number of points, i.e.,  $2q$ , to preserve the drop shape in the equilibrium state.

To confirm that the flat solution is an equilibrium solution for  $q = 18$  in three-dimensional space, we compute the temporal evolution of the total energy, i.e.,

$$\mathcal{E}(\phi) = \int_0^1 \left[ F(\phi) + \frac{\epsilon^2}{2} \phi_r^2 \right] 4\pi r^2 dr.$$

The discrete total energy is defined as

$$\mathcal{E}^h(\phi^n) = 4\pi \sum_{i=1}^{N_r} \left[ F(\phi_i^n) r_i^2 + \frac{\epsilon^2}{2} \left( \frac{\phi_{i+1}^n - \phi_i^n}{h} \right)^2 r_{i+\frac{1}{2}}^2 \right] h.$$

In this test, we consider the evolution of the numerical solution of the CH equation and the temporal evolution of total energy in a three-dimensional domain for  $q = 18$ . The parameters for the same are selected as follows:  $h = 1/64$ ,  $\epsilon = \epsilon_4$ ,  $\Delta t = 0.1h^2$ . We consider the initial condition to be

$$\phi(r, 0) = \begin{cases} 1, & \text{if } r \leq 18h, \\ -1, & \text{otherwise,} \end{cases} \quad (3.2)$$

in the computational domain  $\Omega = (0, 1)$ . Fig. 3(a) shows the evolution of the numerical solution of the CH equation for  $q = 18$ ; the direction of the arrow shows the direction of evolution of the numerical solutions, and (b) shows the temporal evolution of the normalized total energy,  $\mathcal{E}^h(\phi^n)/\mathcal{E}^h(\phi^0)$ . We can infer from the figure that the total energy of the CH equation decreases with increasing time.

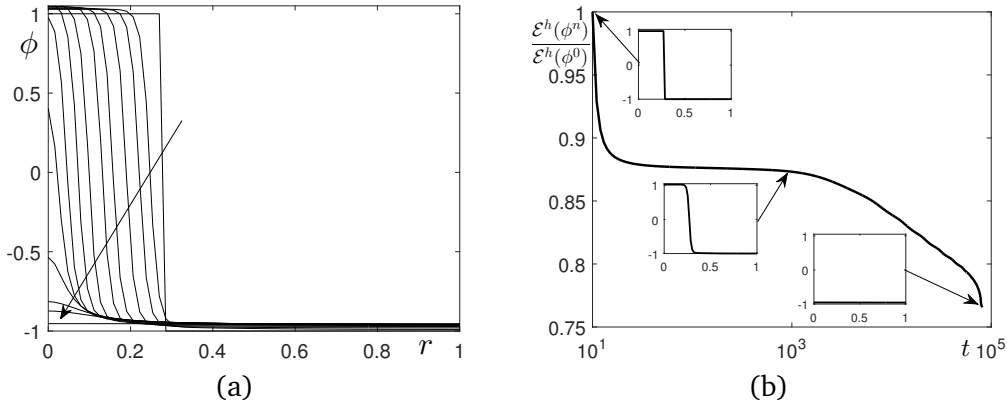


Figure 3: (a) The evolution of the numerical solution of the CH equation. The arrow indicates the direction of evolution. (b) The temporal evolution of the normalized total energy,  $\mathcal{E}^h(\phi^n)/\mathcal{E}^h(\phi^0)$ .

### 3.2. Conservative Allen–Cahn equation

Next, we consider the CAC equation. We use the same initial condition (3.1), with  $q = 7$  and  $\epsilon_4$ . Figs. 4(a), (b), and (c) show the one-, two-, and three-dimensional numerical equilibrium solutions with different values of  $q$ , respectively. From the results, we can conclude that non-constant solutions exist in the two-dimensional space, except for  $q = 1$ , and in the three-dimensional space, except for  $q = 1, 2$ .

Fig. 5(a) shows a comparison between the equilibrium solutions of one-, two-, and three-dimensional space with  $q = 19$ . The equilibrium profiles for all dimensions are almost identical. Fig. 5(b) shows the temporal evolution of the numerical solution in three-dimensional space. The arrows indicate the direction of evolution. Unlike the solution from the CH equation, the zero-level set of the phase-field does not deviate from the initial location.

Table 2 lists  $(p, q)$  for various  $\epsilon$  values, where  $p$  is the number of grid points satisfying  $\phi \geq -0.9$ , and  $q$  is the minimum value of the integer that preserves a drop shape in equilibrium state. Compared with the results from the CH equation, we need considerably fewer grid points to preserve a drop shape in equilibrium state.

Table 2:  $(p, q)$  for various  $\epsilon$  values, where  $p$  is the number of grid points satisfying  $\phi \geq -0.9$ , and  $q$  is the minimum value of the integer that preserves a drop shape in equilibrium state.

Case	$\epsilon = \epsilon_4$	$\epsilon = \epsilon_6$	$\epsilon = \epsilon_8$	$\epsilon = \epsilon_{10}$	$\epsilon = \epsilon_{12}$
1D	(3, 1)	(5, 1)	(7, 1)	(9, 1)	(9, 1)
2D	(4, 2)	(6, 3)	(8, 4)	(10, 4)	(12, 5)
3D	(5, 3)	(6, 4)	(9, 6)	(11, 7)	(13, 8)

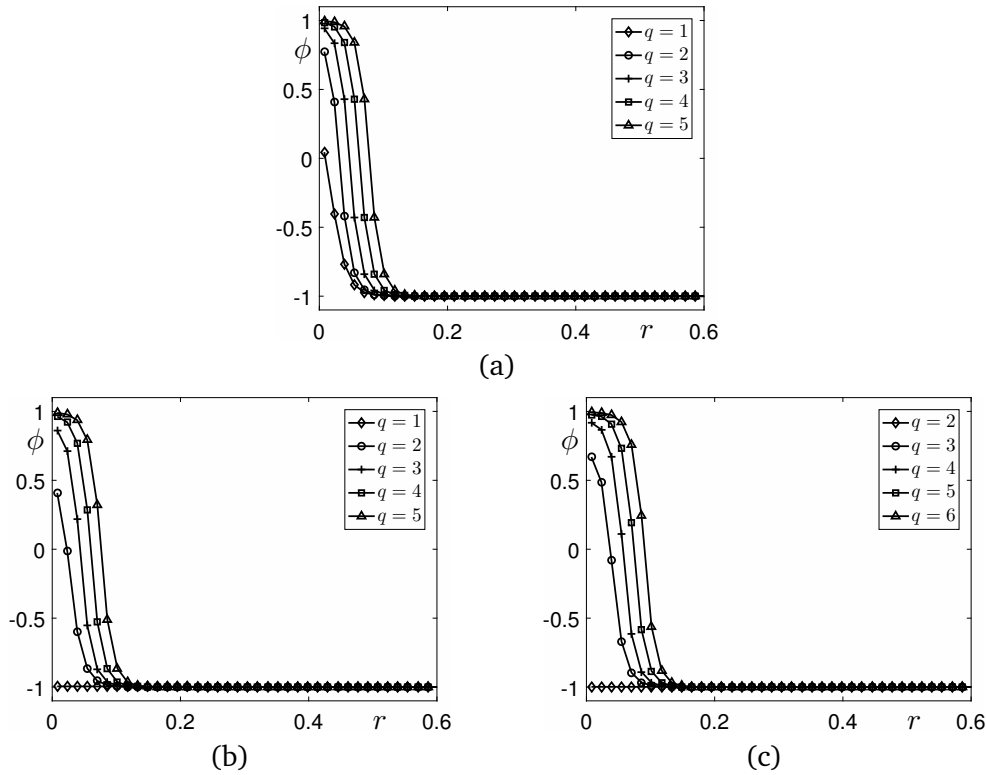


Figure 4: (a), (b), and (c) depict the one-, two-, and three-dimensional numerical equilibrium solutions with different values of  $q$ , respectively.

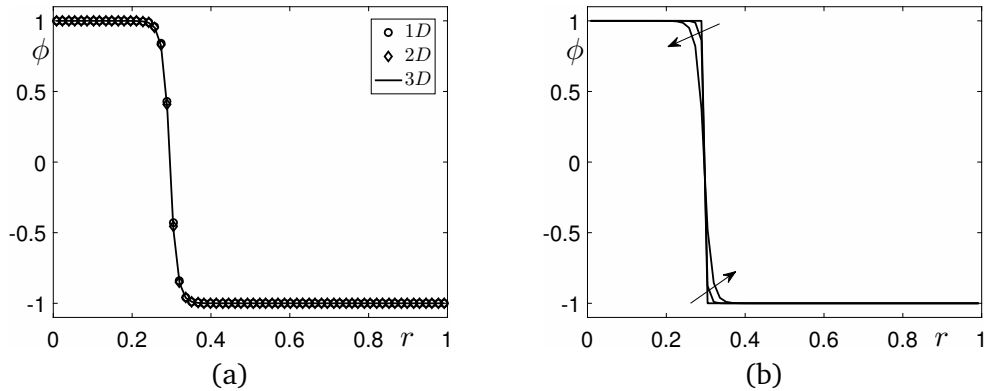


Figure 5: (a) Comparison between equilibrium solutions of one-, two-, and three-dimensional space with  $q = 19$ . (b) Temporal evolution of the numerical solution in three-dimensional space. The arrows indicate the direction of evolution.

### 3.3. Comparison between CH and CAC equations

Fig. 6 shows a comparison between the equilibrium solutions of the CH (dashed line) and CAC (solid line) equations in three-dimensional space with  $q = 19$ . We can

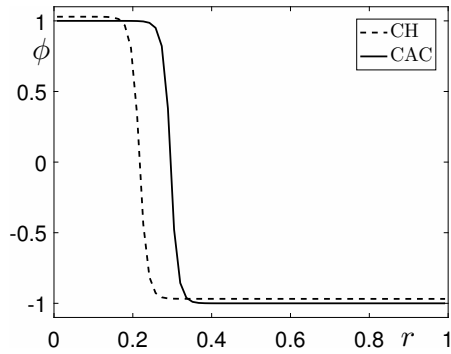


Figure 6: Comparison between equilibrium solutions of the CH (dashed line) and CAC (solid line) equations in three-dimensional space with  $q = 19$ .

observe a severe shrinkage in the result of the CH equation, compared with that of the CAC equation.

### 3.4. Comparison between the two models using two-phase fluid flows

A typical equation for analyzing fluid flow is the Navier–Stokes (NS) equation. The NS equation continues to be the focus of various studies [21, 22]. We consider two-phase fluid flows with the CH and CAC equations. The Navier–Stokes–Cahn–Hilliard (NSCH) system is given by

$$\mathbf{u}_t + \mathbf{u} \cdot \nabla \mathbf{u} = -\nabla p + \frac{1}{Re} \Delta \mathbf{u} + \frac{1}{We} \mathbf{SF}, \tag{3.3a}$$

$$\nabla \cdot \mathbf{u} = 0, \tag{3.3b}$$

$$\phi_t + \nabla \cdot (\phi \mathbf{u}) = \frac{1}{Pe} \Delta \mu, \tag{3.3c}$$

$$\mu = F'(\phi) - \epsilon^2 \Delta \phi, \tag{3.3d}$$

where  $\mathbf{u}$  is the velocity,  $p$  is the pressure, and  $\mathbf{SF}$  is the surface-tension force. There are several different forms for representing the surface-tension force [23]. In this study, we consider

$$\mathbf{SF} = -0.75\sqrt{2}\epsilon \nabla \cdot (\nabla \phi / |\nabla \phi|) |\nabla \phi| \nabla \phi.$$

The non-dimensional parameters are the Reynolds number  $Re$ , Weber number  $We$ , and Peclet number  $Pe$ .

The Navier–Stokes–conservative Allen–Cahn (NSCAC) system is given by

$$\mathbf{u}_t + \mathbf{u} \cdot \nabla \mathbf{u} = -\nabla p + \frac{1}{Re} \Delta \mathbf{u} + \frac{1}{We} \mathbf{SF}, \tag{3.4a}$$

$$\nabla \cdot \mathbf{u} = 0, \tag{3.4b}$$

$$\phi_t + \nabla \cdot (\phi \mathbf{u}) = \frac{1}{Pe} \left( -\frac{F'(\phi)}{\epsilon^2} + \Delta \phi + \beta \sqrt{F(\phi)} \right). \tag{3.4c}$$

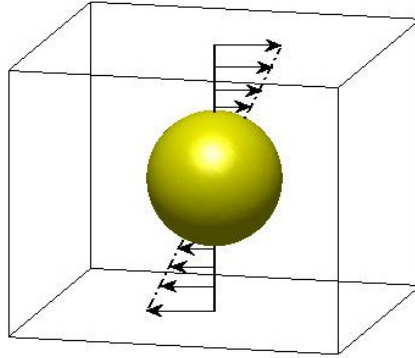


Figure 7: Schematic illustration of a droplet under shear flow.

Both systems have been extensively studied [24–27]. The numerical solutions for the NSCH and NSCAC systems are available in [25, 28], respectively. Here, we consider droplet evolution under simple a shear flow, a schematic diagram of which is shown in Fig. 7.

In this test, we first consider the shear flow governed by the NSCH system in the computational domain  $\Omega = (-1, 1) \times (-0.5, 0.5) \times (-0.5, 0.5)$  with the parameters as follows:  $h = 1/64$ ,  $\Delta t = 5h^2$ ,  $Re = 200$ ,  $We = 50$ ,  $\epsilon = \epsilon_4$ , and  $Pe = 1/\epsilon$ . We consider the following initial condition:

$$\phi = \tanh\left(\frac{0.2 - \sqrt{r}}{\sqrt{2}\epsilon}\right), \quad u = z, \quad v = 0, \quad w = 0,$$

where  $r = \sqrt{x^2 + y^2 + z^2}$  denotes the distance from the center. The parameters  $u$ ,  $v$ , and  $w$  denote the velocity in the  $x$ -,  $y$ -, and  $z$ -directions, respectively. Figure 8(a) shows the temporal evolution of a droplet under a simple shear flow in three-dimensional space at  $t = 0$ ,  $16000\Delta t$ ,  $17000\Delta t$ , and  $17200\Delta t$ . The corresponding temporal evolution of the cross-sectional slice of the droplet with the velocity field is shown in Fig. 9(a). We can observe that the size of the droplet is vanishing with the passage of time. In Fig. 1(d), we find that the initial droplet will decrease and eventually disappears if  $q \leq 18$ , i.e., the initial radius of droplet is less than or equal to the length of 18 grid points in 3D space. We plot the half cross profile of Fig. 9(a) in Fig. 10 and we can find that the initial radius is less than the length of 18 grid points. Therefore, the CH model can not preserve the volume of droplet.

Next, we investigate the two-phase fluid flow governed by the NSCAC system. The computational domain, the initial condition, and the parameters are taken to be the same as for the previous case, except for the Peclet number,  $Pe = 0.001/\epsilon$ . Fig. 8(b) shows the temporal evolution of the droplet in a three-dimensional space. The corresponding temporal evolution of the cross-sectional slice of the droplet is shown in Fig. 9(b). The first, second, third, and fourth rows represent the initial condition and snapshots of the numerical results at  $t = 16000\Delta t$ ,  $17000\Delta t$ , and  $17200\Delta t$ , respectively.

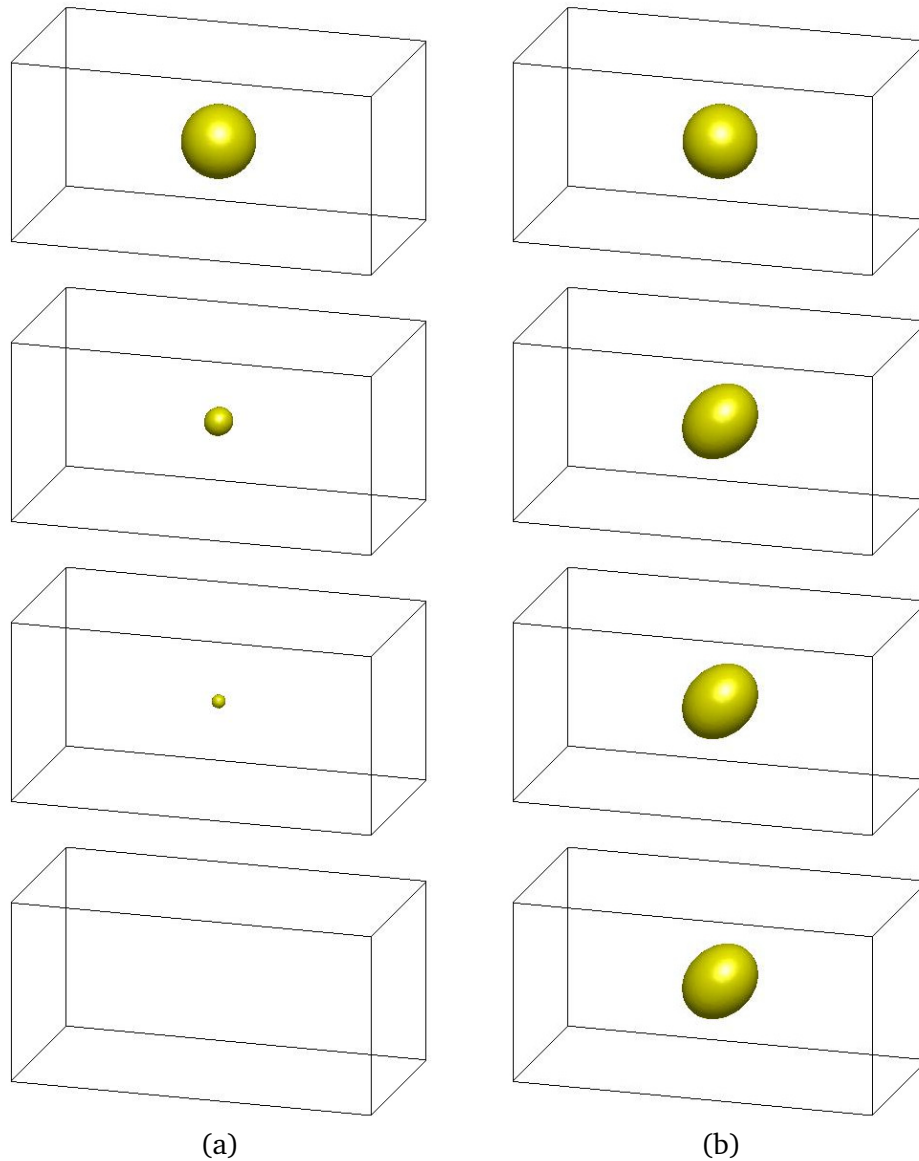


Figure 8: Temporal evolution of a droplet under a simple shear flow. (a) NSCH system and (b) NSCAC system. The first, second, third, and fourth rows depict the initial condition and snapshots of the numerical results at  $t = 16000\Delta t$ ,  $17000\Delta t$ , and  $17200\Delta t$ , respectively.

We can observe that the droplet conserves its original volume during the temporal evolution.

Now, we investigate the large deformation of a droplet under a shear flow for the NSCH and NSCAC models. To show the dynamics of the CH equation without flow, we set an initial droplet at the center of the domain,  $\Omega = (0, 2) \times (0, 1) \times (0, 1)$ , with two different radii,  $R_1 = 0.2$  and  $R_2 = 0.35$ . We use  $h = 1/64$ ,  $\Delta t = 0.01$ ,  $Pe = 1$ ,  $\epsilon = \epsilon_4$ .

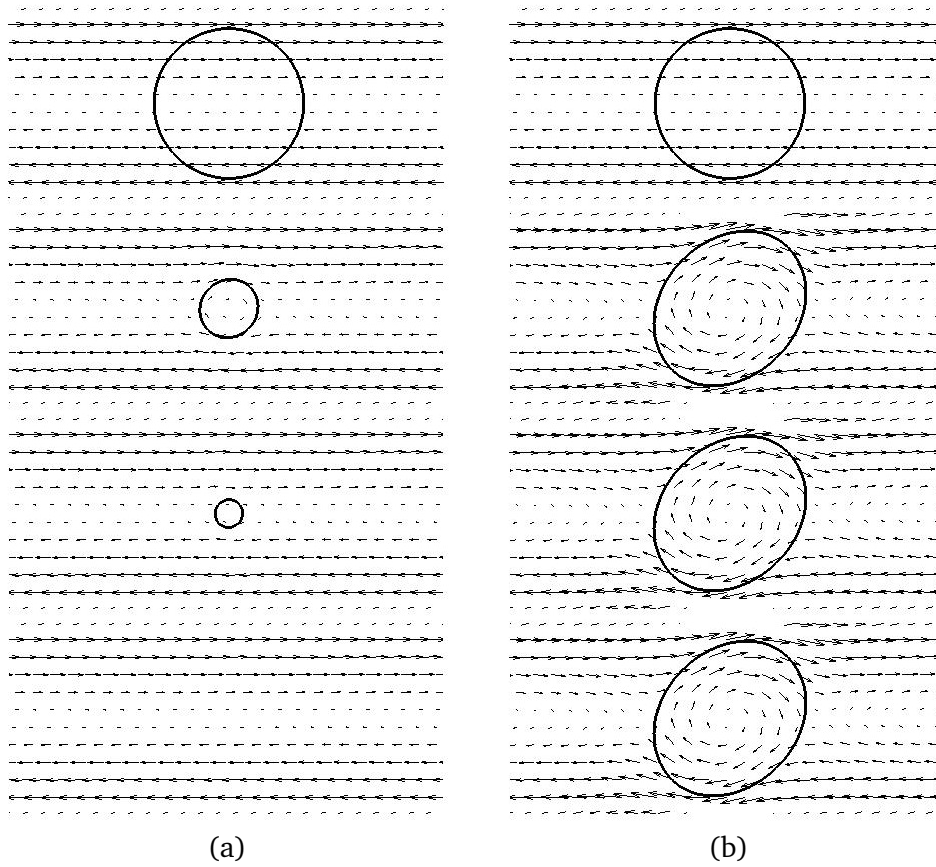


Figure 9: Cross-sectional slice in  $x - z$  plane through  $y = 0$  after various time steps. (a) NSCH system and (b) NSCAC system. The first, second, third, and fourth rows depict the initial condition and snapshots of the numerical results at  $t = 16000\Delta t$ ,  $17000\Delta t$ , and  $17200\Delta t$ , respectively.

Figs. 11(a) and (b) show the evolutions of droplet according to the CH dynamics. We find that the droplet having radius  $R_2 = 0.35$  sustains itself for a long time, whereas the droplet having radius  $R_1 = 0.2$  vanishes within a short time. In the following test, we use the radius  $R_2 = 0.35$  for the NSCH and NSCAC models.

For the NSCH and NSCAC models, the initial conditions are given as

$$\begin{aligned}\phi(x, y, z, 0) &= \tanh\left(\frac{0.35 - \sqrt{(x-1)^2 + (y-0.5)^2 + (z-0.5)^2}}{\sqrt{2}\epsilon}\right), \\ u(x, y, z, 0) &= 4(y-0.5), \\ v(x, y, z, 0) &= 0, \\ p(x, y, z, 0) &= 0,\end{aligned}$$

in the domain  $\Omega = (0, 2) \times (0, 1) \times (0, 1)$ . The numerical parameters are  $h = 1/64$ ,  $Re = 50$ ,  $\Delta t = 5h^2$ ,  $We = 100$ ,  $\epsilon = \epsilon_4$ , and  $Pe = 1/\epsilon$ . Figs. 12(a) and (b) show the

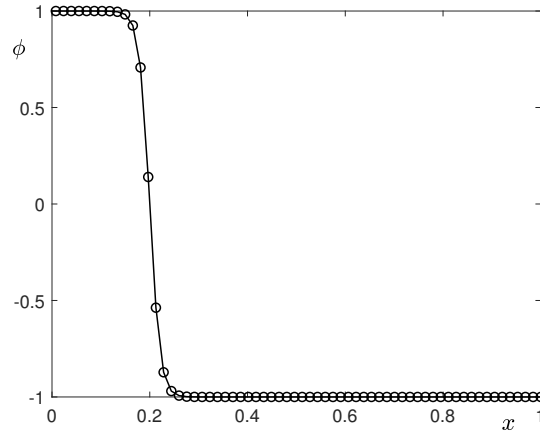


Figure 10: Half cross profile of Fig. 9(a).

evolution of droplet deformation for the NSCH model and the NSCAC model, respectively. The temporal evolutions of the non-dimensional discrete volume of a droplet for the two types of models are shown in Fig. 13. In the case of large deformation, the non-dimensional discrete volume of a droplet for the NSCAC model is almost entirely conserved, whereas the non-dimensional discrete volume of a droplet for the NSCH model decreases with the passage of time. Thus, the NSCAC model conserves the mass better than the NSCH model does, for the deformation of a single droplet.

### 3.5. CPU time for the CH and the CAC equations

In this part, we investigate the consumed CPU time for the CH and the CAC equations in 3D space. The initial condition is set to be 1 inside a cube with length:  $l = 0.3$  and  $-1$  in the rest region. The computational domain is  $\Omega = (0, 1) \times (0, 1) \times (0, 1)$  with the mesh size:  $h = 1/64$ . We fix the time step:  $\Delta t = 0.1h^2$  and use  $Pe = 1$ ,  $\epsilon = \epsilon_8$ . Figs. 14(a) and (b) show the temporal evolutions of CH and CAC equations, respectively. The consumed CPU time is illustrated in Fig. 15. As we can see, the calculation of CH equation costs more time than the CAC equation.

### 3.6. Equilibrium states of the CH and the CAC equations with a logarithm potential

We further investigate the effect of initial conditions on the equilibrium states of the CH and the CAC equations with the following physically relevant logarithm potential [29]:

$$F(\phi) = \frac{\theta}{2} \left[ (1 + \phi) \ln \left( \frac{1 + \phi}{2} \right) + (1 - \phi) \ln \left( \frac{1 - \phi}{2} \right) \right] + \frac{\theta_c}{2} (1 - \phi^2),$$

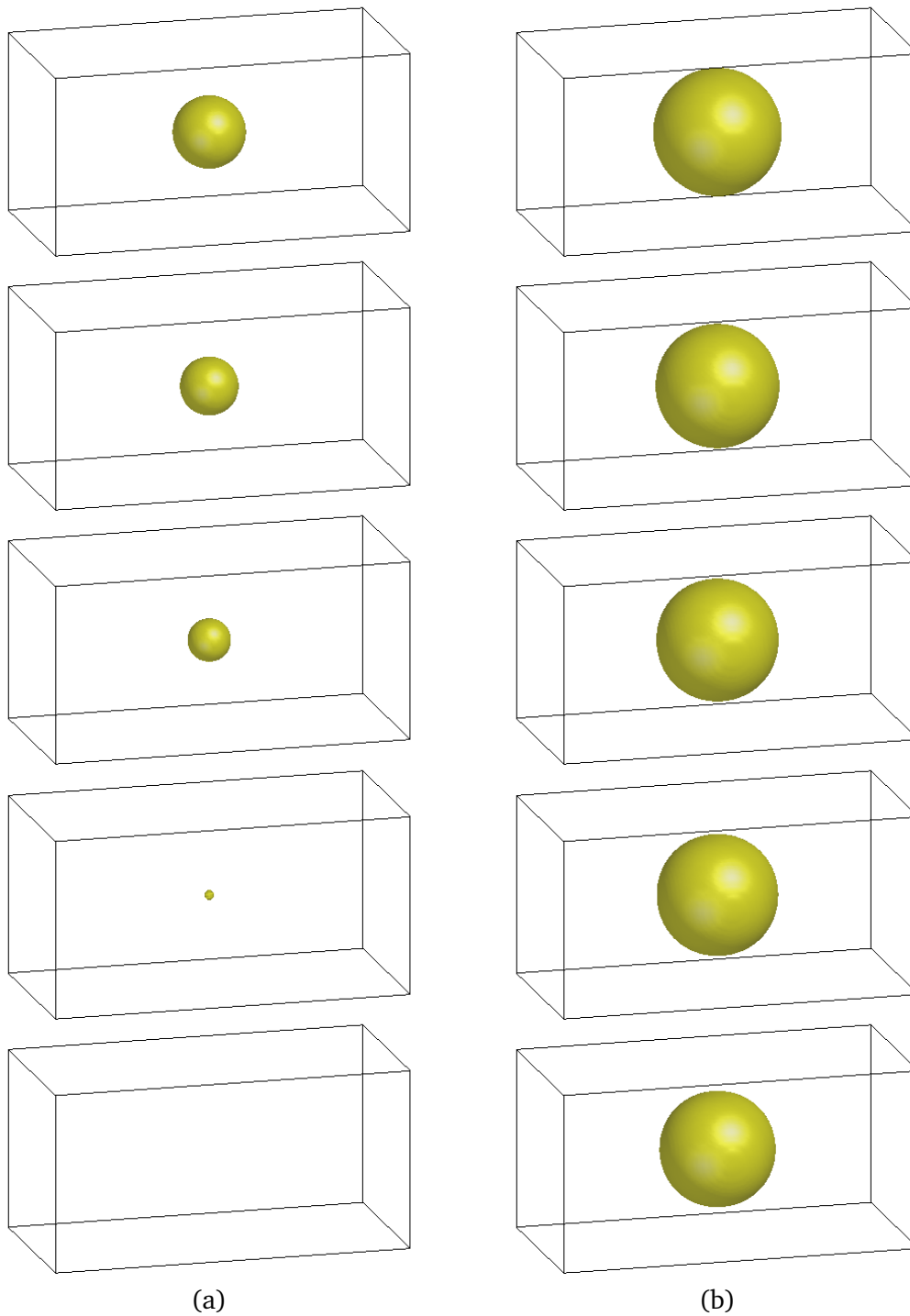


Figure 11: Temporal evolution of droplets with different radii. (a)  $R_1 = 0.2$ , (b)  $R_2 = 0.35$ . The dimensionless times from top to bottom for each column are  $t = 0, 0.4, 0.9, 1.3, 4.0$ .

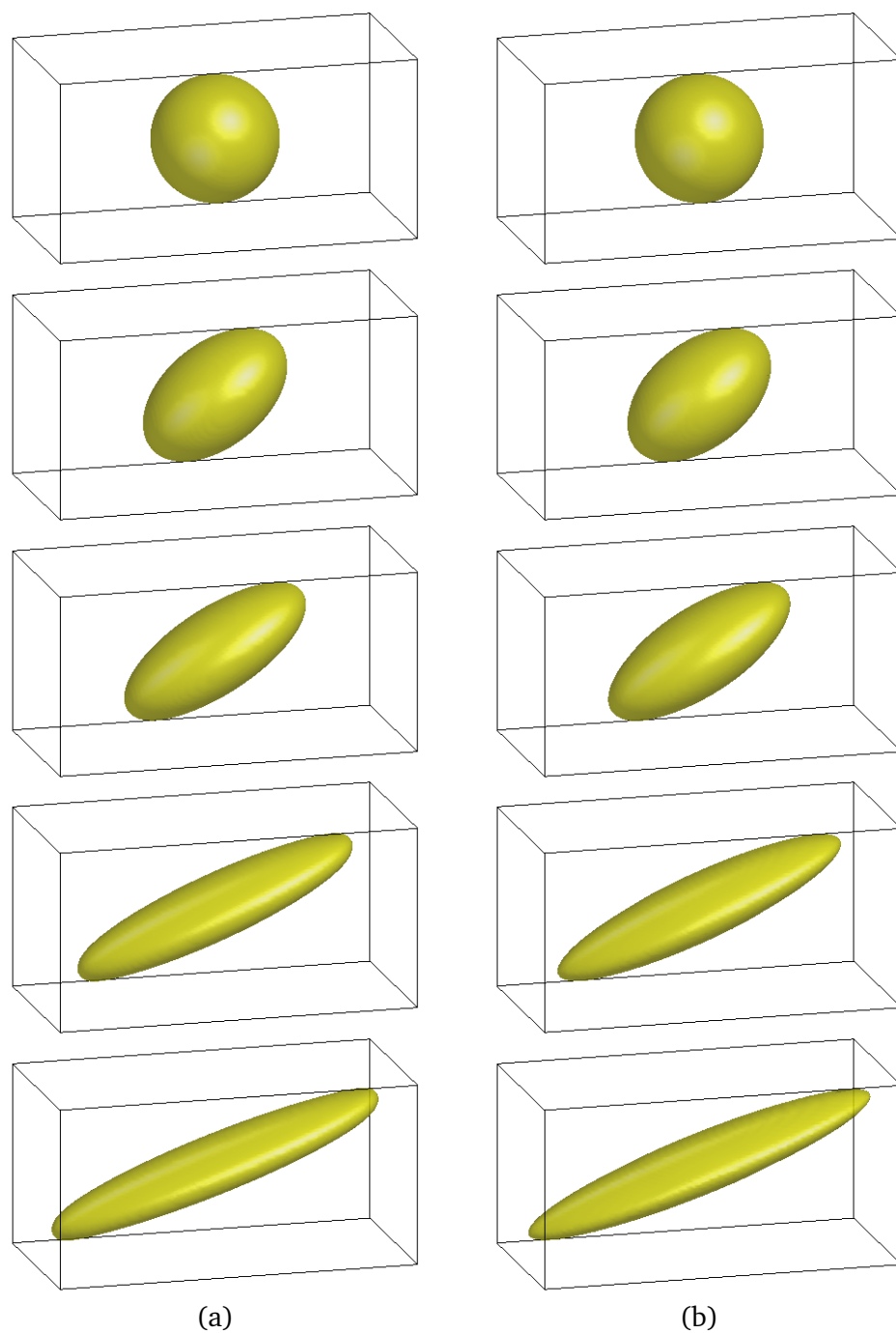


Figure 12: Temporal evolutions of droplet deformation for (a) NSCH model and (b) NSCAC model. The dimensionless times from the top to bottom for each column are  $t = 0, 0.134, 0.2686, 0.5249, 0.6592$ .

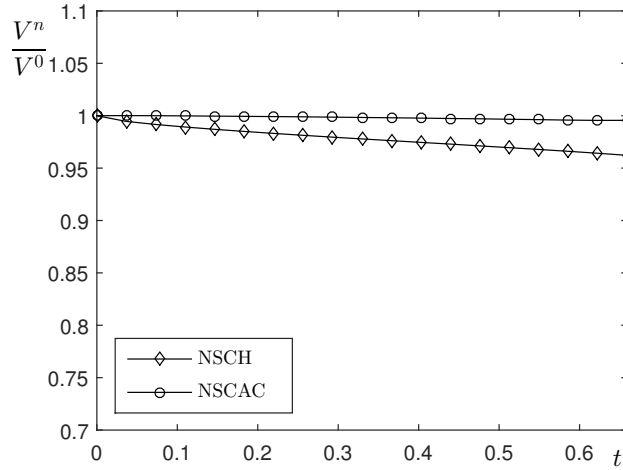


Figure 13: Temporal evolutions of non-dimensional discrete volume of a droplet for NSCH and NSCAC models.

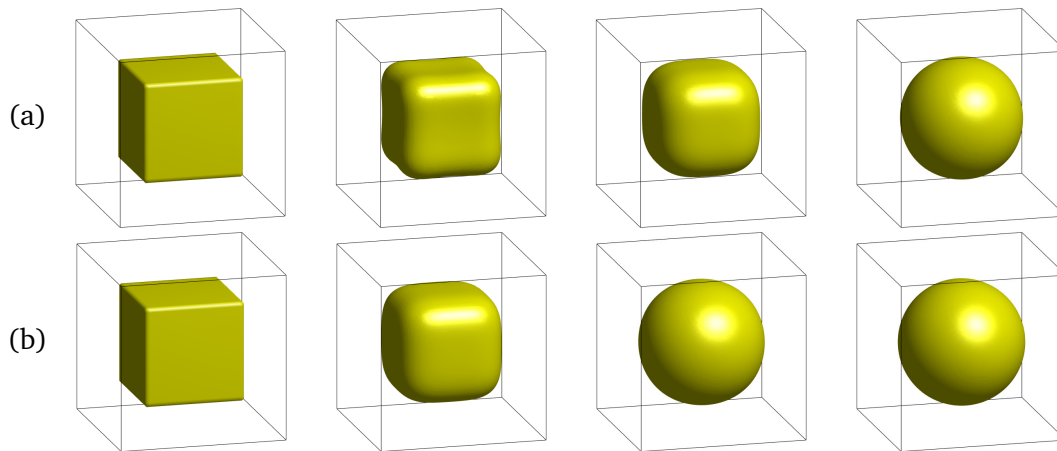


Figure 14: Temporal evolutions of (a) CH equation and (b) CAC equation. The last figure in each row is the numerical equilibrium state.

where  $\theta$  is an absolute temperature and  $\theta_c$  is a critical temperature. In this test, we use  $\theta = 0.6$  and  $\theta_c = 1$ . Lee and Kim [29] found that a proper value of parameter  $\epsilon$  was related to the absolute temperature  $\theta$  and the number of grid points lying in the interfacial layer. Thus, if we use the  $\theta$  value and want  $m$  grid points to lie in the interfacial layer, the formula is given by:

$$\epsilon(\theta, m) = 0.1h(4.835\theta^2 + 0.005m^2 - 3.752\theta m - 4.01\theta + 4.078m + 0.693).$$

Here, we use

$$\epsilon = \epsilon(0.6, 4), \quad h = 1/64 \quad \text{and} \quad \Delta t = 0.1h^2$$

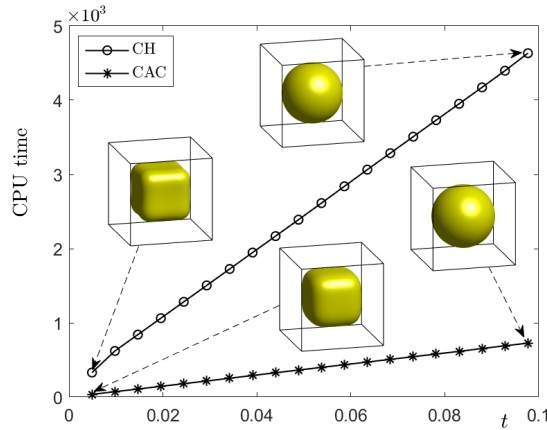


Figure 15: Consumed CPU time for the CH and CAC equations. The insets are the evolutions at specific moments.

in the domain  $\Omega = (0, 1)$ . We take the following initial condition:

$$\phi(r, 0) = \begin{cases} 0.9, & \text{if } r \leq qh, \\ -0.9, & \text{otherwise.} \end{cases}$$

The equilibrium states with respect to different initial conditions are shown in Fig. 16, where the first row and second row represent the results of CH and CAC equations, respectively. In each row, the figures from the left to right are the results in 1D, 2D, and 3D, respectively. As we can observe, the minimum number of  $q$  which yields a non-constant solution increases as the space dimension increases from 1D to 3D, i.e.,  $q = 2$ ,  $q = 8$ , and  $q = 15$  for the CH equation,  $q = 2$ ,  $q = 8$ , and  $q = 14$  for the CAC equation.

#### 4. Conclusions

In this work, we numerically studied the effect of space dimensions on the equilibrium solutions of the CH and CAC equations in one, two, and three dimensions. In general, to obtain non-constant solutions, more grid points are needed with increasing space dimensions for both the equations. However, this tendency is more evident in the CH equation than in the CAC equation, especially in the three-dimensional space. Therefore, although both the equations conserve the total mass, we may prefer one model over the other one depending on the intended physical applications. We conclude that the three-dimensional CAC equation can be applied to model a two-phase fluid with a droplet [30].

We note that the fractional power in time-fractional phase-field equations can affect the relaxation time reaching the equilibrium as observed in [31]. The effect of the fractional power in time-fractional CH and CAC equations can be considered as the scope of future research.

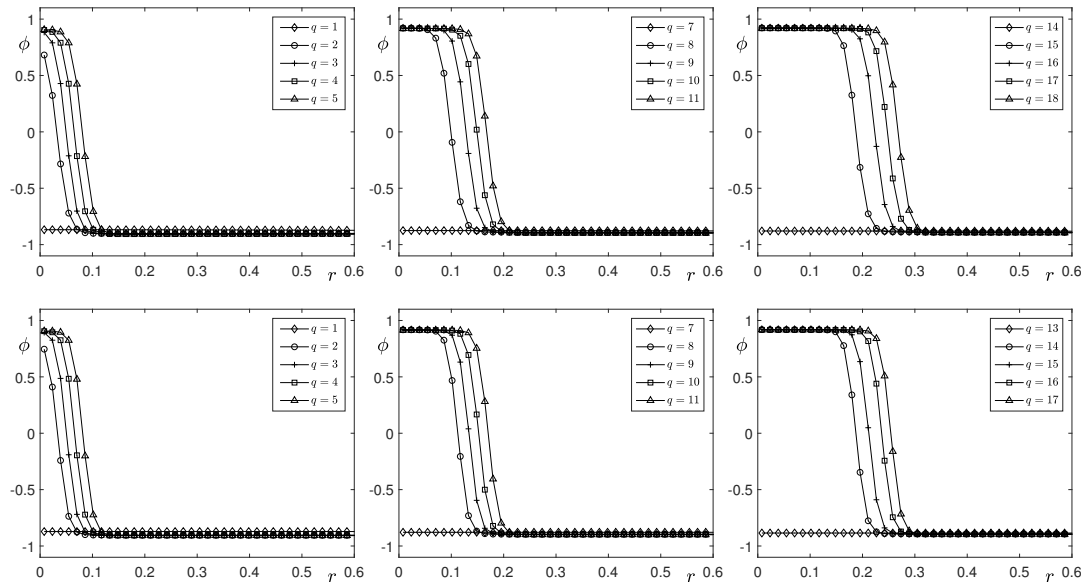


Figure 16: Numerical equilibrium solutions with respect to different values of  $q$ . The first row and the second row are the results of CH and CAC equations. The figures from the left to right in each row are the results in 1D, 2D, and 3D, respectively.

**Acknowledgements** The first author (H. G. Lee) is supported by Basic Science Research Program through the National Research Foundation of Korea (NRF) funded by the Ministry of Education (NRF-2019R1C1C1011112). The corresponding author (J. S. Kim) was supported by Basic Science Research Program through the National Research Foundation of Korea (NRF) funded by the Ministry of Education (NRF-2019R1A2C1003053).

## References

- [1] J.W. CAHN AND J.E. HILLIARD, *Free Energy of a nonuniform system. I. Interfacial free energy*, J. Chem. Phys., 58 (1958), pp. 258–267.
- [2] D. LEE, J.Y. HUH, D. JEONG, J. SHIN, A. YUN AND J. KIM, *Physical, mathematical, and numerical derivations of the Cahn–Hilliard equation*, Comput. Mater. Sci., 81 (2014), pp. 216–225.
- [3] M. BRASSEL AND E. BRETIN, *A modified phase field approximation for mean curvature flow with conservation of the volume*, Math. Methods Appl. Sci., 34 (2011), pp. 1157–1180.
- [4] S. PEI, Y. HOU AND B. YOU, *A linearly second-order energy stable scheme for the phase field crystal model*, Appl. Numer. Math., 140 (2019), pp. 134–164.
- [5] L. WANG AND H. YU, *On efficient second order stabilized semi-implicit schemes for the Cahn–Hilliard phase-field equation*, J. Sci. Comput., 77 (2018), pp. 1185–1209.
- [6] Y. LI AND J. KIM, *An efficient and stable compact fourth-order finite difference scheme for the phase crystal equation*, Comput. Method Appl. M., 319 (2016), pp. 194–216.

- [7] Y. DENG, Z. LIU AND Y. WU, *Topology optimization of capillary, two-phase flow problems*, Commun. Comput. Phys., 22 (2017), pp. 1413–1438.
- [8] M. DEGHAN AND V. MOHAMMADI, *Comparison between two meshless methods based on collocation technique for the numerical solution of four-species tumor growth model*, Commun. Nonlinear Sci., 44 (2017), pp. 204–219.
- [9] W. YANG, Z. HUANG AND W. ZHU, *Image Segmentation Using the Cahn–Hilliard equation*, J. Sci. Comput., <http://doi.org/10.1007/s10915-018-00899-7>, (2019).
- [10] M. FABRIZIO, F. FRANCHI, B. LAZZARI AND R. NIBBI, *A non-isothermal compressible Cahn–Hilliard fluid model for air pollution phenomena*, Phys. D., 378 (2018), pp. 46–53.
- [11] L. Ó. NÁRAIGH, *Travelling-wave spatially periodic forcing of asymmetric binary mixtures*, Phys. D., 393 (2019), pp. 24–37.
- [12] D. LEE AND J. KIM, *Comparison study of the conservative Allen–Cahn and the Cahn–Hilliard equations*, Math. Comput. Simul., 119 (2016), pp. 35–56.
- [13] D. J. EYRE, *An unconditionally stable one-step scheme for gradient systems*, preprint. Available from, <http://www.math.utah.edu/~eyre/research/methods/stable.ps>.
- [14] U. TROTTEBERG, A. SCHÜLLER AND C. OOSTERLEE, *Multigrid*, Academic Press, London, 2011.
- [15] J. KIM, *A numerical method for the Cahn–Hilliard equation with a variable mobility*, Commun. Nonlinear Sci., 12 (2007), pp. 1560–1571.
- [16] Y. LI, H. G. LEE, B. XIA AND J. KIM, *A compact fourth-order finite difference scheme for the three-dimensional Cahn–Hilliard equation*, Comput. Phys. Commun., 200 (2016), pp. 108–116.
- [17] J. KIM, S. LEE AND Y. CHOI, *A conservative Allen–Cahn equation with a space-time dependent Lagrange multiplier*, Int. J. Eng. Sci., 84 (2014), pp. 11–17.
- [18] H. G. LEE, *High-order and mass conservative methods for the conservative Allen–Cahn equation*, Comput. Math. Appl., 72 (2016), pp. 620–631.
- [19] J. M. CHURCH, Z. GUO, P. K. JIMACK, A. MADZVAMUSE, K. PROMISLOW, B. WETTON, S. M. WISE AND F. YANG, *High accuracy Benchmark problems for Allen–Cahn and Cahn–Hilliard dynamics*, Commun. Comput. Phys., 26 (2019), pp. 947–972.
- [20] J. W. CHOI, H. G. LEE, D. JEONG AND J. KIM, *An unconditionally gradient stable numerical method for solving the Allen–Cahn equation*, Phys. A, 388 (2009), pp. 1791–1803.
- [21] T. WANG AND T. LIU, *A consistent fourth-order compact finite difference scheme for solving vorticity-stream function form of incompressible Navier–Stokes equations*, Numer. Math. Theor. Meth. Appl., 12 (2018), pp. 312–330.
- [22] M. N. ASIAM, J. ZHANG, N. DANG AND R. AHMAD, *An improved model reduction method on AIMS for NS equations using multilevel finite element method and hierarchical basis*, Numer. Math. Theor. Meth. Appl., 12 (2019), pp. 115–133.
- [23] J. KIM, *A continuous surface tension force formulation for diffuse-interface models*, J. Comput. Phys., 204 (2005), pp. 784–804.
- [24] M. HEIDA, *On the derivation of thermodynamically consistent boundary conditions for the Cahn–Hilliard–Navier–Stokes system*, Int. J. Eng. Sci., 62 (2013), pp. 126–156.
- [25] D. JEONG AND J. KIM, *Conservative Allen–Cahn–Navier–Stokes system for incompressible two-phase fluid flows*, Comput. Fluids, 156 (2017), pp. 239–246.
- [26] A. GIORGINI, A. MIRANCILLE AND R. TEMAM, *Uniqueness and regularity for the Navier–Stokes–Cahn–Hilliard system*, SIAM J. Math. Anal., 51 (2019), pp. 2535–2574.
- [27] S. AIHARA, T. TAKAKI AND N. TAKADA, *Multi-phase-field modeling using a conservative Allen–Cahn equation for multiphase flow*, Comput. Fluids, 178 (2019), pp. 141–151.
- [28] J. KIM, *Phase-field models for multi-component fluid flows*, Commun. Comput. Phys., 12

- (2012), pp. 613–661.
- [29] H. G. LEE AND J. KIM, *A nonlinear convex splitting Fourier spectral scheme for the Cahn–Hilliard equation with a logarithmic free energy*, Bull. Korean Math. Soc., 56 (2019), pp. 265–276.
- [30] M. SULMAN, *Optimal mass transport-based adaptive mesh method for phase-field models of two-phase fluid flows*, Comput. Math. Appl., 72 (2016), pp. 2181–2193.
- [31] T. TANG, H. YU AND T. ZHOU, *On energy dissipation theory and numerical stability for time-fractional phase-field equations*, SIAM J. Sci. Comput., 41 (2019), pp. A3757–A3778.

Copyright of Numerical Mathematics: Theory, Methods & Applications is the property of Global Science Press and its content may not be copied or emailed to multiple sites or posted to a listserv without the copyright holder's express written permission. However, users may print, download, or email articles for individual use.